

Article

Properties Assessment by Quantum Mechanical Calculations for Azulenes Substituted with Thiophen- or Furan-Vinyl-Pyridine

Oana Ciocirlan ¹, Eleonora-Mihaela Ungureanu ^{2,*}, Alina-Alexandra Vasile (Corbei) ¹ and Amalia Stefaniu ^{3,*}

¹ Department of Inorganic Chemistry, Physical Chemistry and Electrochemistry, Faculty of Applied Chemistry and Materials Science, University POLITEHNICA of Bucharest, Gheorghe Polizu 1-7, Sector 1, 011061 Bucharest, Romania; ciocirlan_o@yahoo.com (O.C.); vasilecalinaalexandra@yahoo.com (A.-A.V.)

² Doctoral School "Applied Chemistry and Materials Science", University POLITEHNICA of Bucharest, 011061 Bucharest, Romania

³ National Institute of Chemical, Pharmaceutical Research and Development, Bucharest, Vitan Av. 112, Sector 3, 031299 Bucharest, Romania

* Correspondence: em_ungureanu2000@yahoo.com (E.-M.U.); mihaela.ungureanu@upb.ro or astefaniu@gmail.com (A.S.)

Abstract: In this paper, azulenes substituted with thiophen- or furan-vinyl-pyridine are reported as heavy metal ligands in systems based on chemically modified electrodes. We undertook a computational study of their structures using density functional theory (DFT). Based on these computations, we obtained properties and key molecular descriptors related to chemical reactivity and electrochemical behavior. We investigated the correlation between some quantum parameters associated with the chemical reactivity and the complexing properties of the modified electrodes based on these ligands. The best correlations for the parameters were retained. We showed that the linear correlation between DFT-computed HOMO/LUMO energies and experimental redox potentials is very good.

Keywords: thiophen-vinyl-pyridine-azulenes; furan-vinyl-pyridine-azulenes; quantum mechanical calculations; DFT; electrochemical properties; reactivity parameters



Citation: Ciocirlan, O.; Ungureanu, E.-M.; Vasile (Corbei), A.-A.; Stefaniu, A. Properties Assessment by Quantum Mechanical Calculations for Azulenes Substituted with Thiophen- or Furan-Vinyl-Pyridine. *Symmetry* **2022**, *14*, 354. <https://doi.org/10.3390/sym14020354>

Academic Editor: Radomir Jasiński

Received: 16 January 2022

Accepted: 8 February 2022

Published: 10 February 2022

Publisher's Note: MDPI stays neutral with regard to jurisdictional claims in published maps and institutional affiliations.



Copyright: © 2022 by the authors. Licensee MDPI, Basel, Switzerland. This article is an open access article distributed under the terms and conditions of the Creative Commons Attribution (CC BY) license (<https://creativecommons.org/licenses/by/4.0/>).

1. Introduction

Chemically modified electrodes (CMEs) obtained by electrochemical polymerization of differently substituted azulene monomers have been previously tested and characterized by electrochemistry [1,2]. The previously reported data refer to heavy metals (HMs) ions recognition attempts to detect very low concentrations of contaminants such as cadmium, copper, mercury, chromium, cobalt, nickel, or lead in water [3–5]. The advantage is certain in the context of health concerns due to the harmful effects of these HMs on humans; their bioaccumulation in the human body causes acute or chronic toxicity, responsible for serious disorders especially at long-term exposure. Indeed, new research connecting the occurrence of progressive physical and neurological degenerative damages such as Parkinson's and Alzheimer's diseases, or even cancer, and HMs accumulation has appeared [6–9]. Although essential heavy metals are the key constituents of several enzymes involved in biochemical processes and exert important physiological functions (e.g., copper as co-factor of oxidative stress-related enzymes [10] or constituent of metalloenzymes responsible for hemoglobin formation [11]), the danger that they become toxic contaminants must be controlled and prevented.

As part of the ongoing interest in developing methodologies for polyfunctionalization of azulenes [12], we investigated the electrochemistry of a series of 4-(azulen-1yl) pyridines (Figure 1). The investigated compounds are furan-vinyl-pyridine-azulenes (**O1–O3**) and thiophen-vinyl-pyridine-azulenes (**S1–S3**). The grafted pyridines were attached in position 1 to 5-isopropyl-3,8-dimethylazulene (**O1** and **S1**), 4,6,8-trimethylazulene (**O2** and **S2**), or azulene (**O3** and **S3**), respectively.

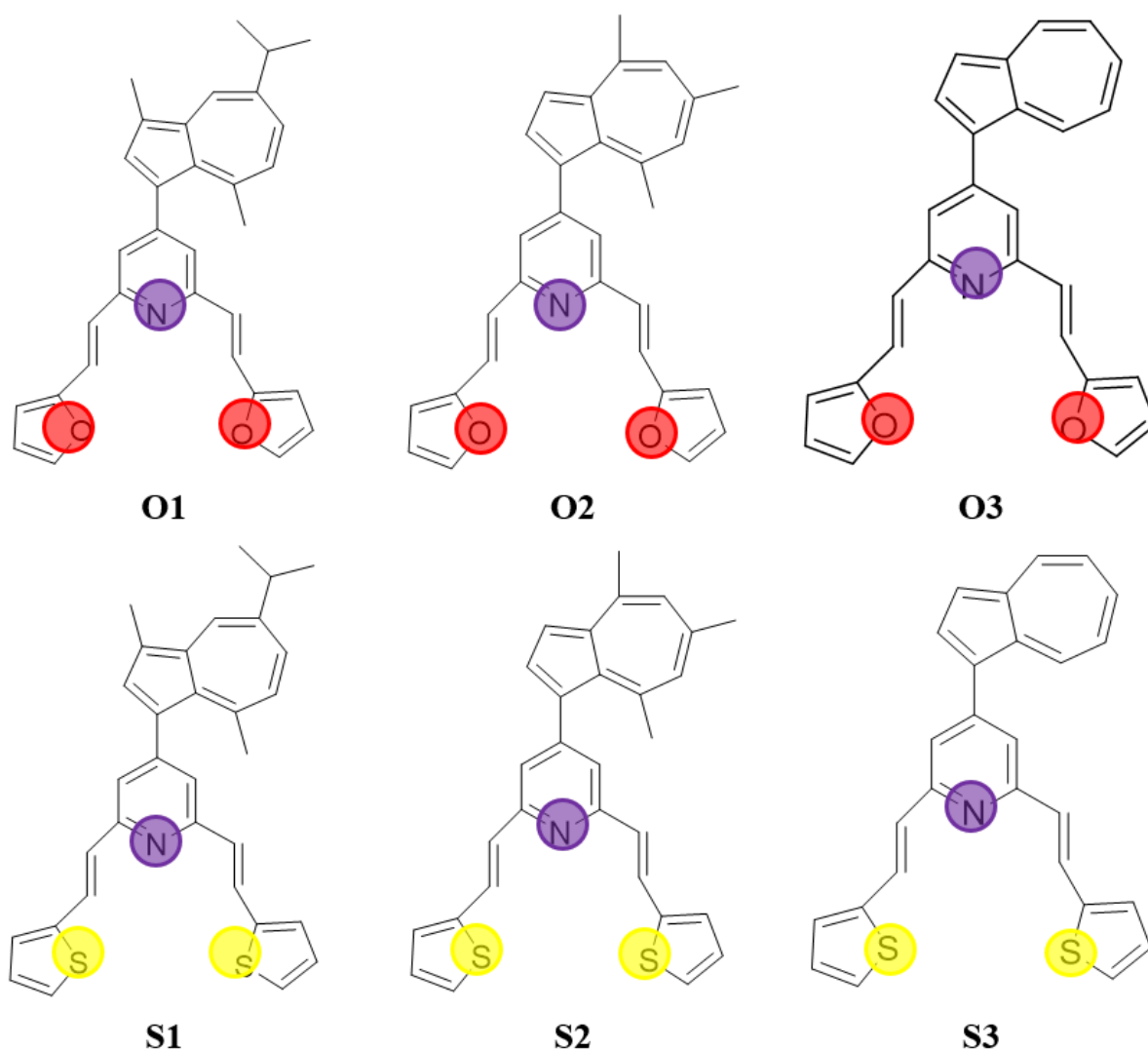


Figure 1. Structures of the studied molecules.

These compounds interact with metal ions due to the property of 2,6-bis((E)-2-(furan/thiophene-2-yl)vinyl)pyridine, which is a Lewis base. They are all valuable synthons for the synthesis of highly conjugated aromatic systems [13,14]. In connection to their capacity to polymerize, they are useful for constructing novel analytical materials for sensor applications [15–17].

The ligands' structures investigated in this paper contain a part of pyridine, known for its HMs complexing properties [18]. The 4-(azulen-1yl) pyridines substituted with furyl–vinyl or thienyl–vinyl lead to more extended conjugated systems, which are easily polymerized. We have previously investigated the electrochemistry of a series of 4-(azulen-1yl) pyridines [19]. Some electrodes based on graphite paste modified with **S2** isomer have shown sensors properties for Zn [20]. The study of **O1** ligand by electrochemical methods led to the finding of the most suitable potential, where this azulene could be polymerized. These modified electrodes were used for HMs recognition through preconcentration and anodic stripping. A good result has been observed for Pb (detection limit of 10^{-7} M) [4]. The electrochemical study of ligand established the best conditions for obtaining CMEs, which were tested for the recognition of HMs cations with good results for lead and for copper at concentrations lower than 10^{-8} M [3]. Modified electrodes based on **O3** and **S3** ligands have been recently reported for HMs ions recognition [21,22]. In order to establish the best ligand for the complexation of HMs (with the lowest detection limits), the estimated chemical parameters are correlated with experimental electrochemical properties [23].

In silico studies of azulenes substituted with thiophen- or furan-vinyl-pyridines were carried out by density functional theory (DFT), aiming to achieve complete structural insights [24,25]. Recent similar data on other azulene structures have revealed linear correlations of DFT-computed energies for frontier molecular orbitals (FMO) and the experimental oxidation and reduction potentials [26]. Thus, the computer-aided investigation has proven a pertinent approach to identify key parameters for designing novel ligands with better electrochemical properties. Generally, previous computations are based on the correlation of electrochemical oxidation and reduction potentials, with energy levels corresponding to the lowest unoccupied molecular orbital (LUMO) or the highest occupied molecular orbital (HOMO), respectively [27–29]. For such quantum computations, the use of the *B3LYP* level of theory has led to strong linear correlations between the energy of the HOMO/LUMO orbitals and redox potentials [30]. More accurate results have been obtained using ω *B97XD* hybrid functional [26,31]. DFT computations provided accurate structural details and prediction properties, which were well correlated with the electrochemical behavior and other properties of the investigated ligands.

2. Computational Details

The properties 'computations and the programs used to depict the molecular electrostatic potential and frontier molecular orbitals surfaces were realized with Spartan 14 software Wavefunction, Inc. Irvine CA, USA [32], for the lowest energy conformers of each structure, in vacuum conditions, at ground state using DFT models [33]. Two levels of theory *B3LYP*—the Becke's three-parameter hybrid exchange functional with the Lee–Yang–Parr correlation functional [34] with basis set 6-31G (d, p) [35,36] and ω *B97XD* with basis set 6-31G (d, p) [37]—were used. In this article, we use the notations *B3LYP* for *B3LYP*/6-31G (d, p) basis set and ω *B97XD* for ω *B97XD*/6-31G (d, p) basis set. QSAR properties were also obtained from Spartan software.

3. Results

3.1. Molecular and QSAR Properties Computations

Table 1 shows the predicted molecular (a–g) and QSAR (h–m) properties resulting from DFT computations using *B3LYP* and ω *B97XD* density functional models for the investigated ligands. In addition to the total energy E (in atomic units, au), estimates are also provided for the energy in water (E_{aq}) and the difference between E_{aq} and E , which represents the solvation energy (E_{solv} in $\text{kJ}\cdot\text{mol}^{-1}$) [38].

Starting from the electronic properties such as E_{HOMO} and E_{LUMO} energies given in Table 1, other related quantum descriptors were calculated. According to Koopman's theorem [39,40], E_{HOMO} is related to the ionization potential ($I = -E_{HOMO}$), and E_{LUMO} to the electron affinity ($A = -E_{LUMO}$). These values are collected in Table 2, together with the HOMO–LUMO energy gap (ΔE_{gap}) values. Additionally, the absolute electronegativity ($\chi = (I + A)/2$), global hardness ($\eta = (I - A)/2$), softness ($\sigma = 1/\eta$) of the ligand molecules [41,42], and global electrophilicity index ($\omega = \mu^2/2\eta$) [43] values are given in Table 2 for oxygen and sulfur compounds.

Variation in values of E_{pot} (Table 1) for each compound can be visualized from the molecular electrostatic potential map (MEP). This is a useful tool in assessing the reactive sites in a molecule [44]. The MEPs for the investigated oxygen compounds are shown in Figure 2, indicating red and blue sites, with negative and positive regions, susceptible to electrophilic and nucleophilic attacks, respectively. The MEPs for the sulfur compounds (S1–S3) are given in Figure 3.

The frontier molecular orbitals density distributions calculated by using *B3LYP*, which resulted from the quantum calculation for oxygen compounds (O1–O3), are represented in Figure 3.3, along with the energy levels and their gaps (ΔE_{gap}) between the HOMO and LUMO (Table 2). Similarly, the representations of FMO density distribution [45] for S1–S3 sulfur compounds are given in Figure 5. The positive and negative phases of the frontier molecular orbitals are represented by red and blue colors, respectively.

Table 1. Predicted molecular ^{a–g} and QSAR ^{h–m} properties of oxygen (O1, O2, O3) and sulfur (S1, S2, S3) compounds calculated using B3LYP and ω B97XD DFT models.

Parameter	O1 C ₃₂ H ₂₉ NO ₂		O2 C ₃₀ H ₂₅ NO ₂		O3 C ₂₇ H ₁₉ NO ₂	
	B3LYP	ω B97XD	B3LYP	ω B97XD	B3LYP	ω B97XD
	<i>M</i> ^a (g·mol ^{−1})	459.59		431.54		389.45
<i>E</i> ^b (au)	−1441.98	−1441.51	−1363.36	−1362.9	−1245.42	−1244.99
<i>E</i> _{aq} ^c (au)	−1441.99	−1441.52	−1363.37	−1362.91	−1245.43	−1245
<i>E</i> _{solv} ^d (kJ·mol ^{−1})	−23.72	−21.35	−27.97	−25.92	−32.7	−30.16
μ ^e (D)	3.10	3.27	3.43	3.67	2.91	3.11
<i>E</i> _{HOMO} ^f (eV)	−4.92	−6.74	−5.08	−6.93	−5.12	−7.03
<i>E</i> _{LUMO} ^g (eV)	−1.79	−0.13	−1.77	−0.13	−2.04	−0.36
<i>S</i> ^h (Å ²)	520.42	514.08	481.21	474.27	429.84	423.09
<i>V</i> ⁱ (Å ³)	508.94	506.68	472.01	469.83	418.75	416.98
<i>PSA</i> ^j (Å ²)	18.27	16.79	18.31	16.80	18.6	17.93
<i>OI</i> ^k	1.69	1.67	1.64	1.62	1.59	1.57
α ^l (10 ^{−30} ·m ³)	81.92	80.91	78.88	77.88	74.61	73.62
<i>E</i> _{pot} ^m (kJ·mol ^{−1})	−166.66	−167.73	−167.67	−168.84	−164.84	−163.65
Parameter	S1 C ₃₂ H ₂₉ NS ₂		S2 C ₃₀ H ₂₅ NS ₂		S3 C ₂₇ H ₁₉ NS ₂	
	B3LYP	ω B97XD	B3LYP	ω B97XD	B3LYP	ω B97XD
	<i>M</i> ^a (g·mol ^{−1})	491.72		463.67		421.59
<i>E</i> ^b (au)	−2087.94	−2087.47	−2009.31	−2008.86	−1891.37	−1890.95
<i>E</i> _{aq} ^c (au)	−2087.95	−2087.48	−2009.32	−2008.88	−1891.38	−1890.96
<i>E</i> _{solv} ^d (kJ·mol ^{−1})	−32.25	−32.25	−36.99	−37.13	−39.55	−38.56
μ ^e (D)	3.11	3.22	3.33	3.55	2.79	2.82
<i>E</i> _{HOMO} ^f (eV)	−4.98	−6.72	−5.13	−6.91	−5.27	−7.07
<i>E</i> _{LUMO} ^g (eV)	−1.84	−0.14	−1.83	−0.14	−2.06	−0.36
<i>S</i> ^h (Å ²)	535.76	532.51	496.12	491.29	444.51	442.36
<i>V</i> ⁱ (Å ³)	526.71	524.23	489.67	487.32	436.52	434.71
<i>PSA</i> ^j (Å ²)	6.297	6.187	6.34	6.21	6.31	6.25
<i>OI</i> ^k	1.70	1.69	1.65	1.64	1.60	1.59
α ^l (10 ^{−30} ·m ³)	83.36	82.34	80.32	79.31	76.03	75.05
<i>E</i> _{pot} ^m (kJ·mol ^{−1})	−160.04	−152.77	−165.18	−154.99	−159.77	−160.26

^a molecular weight (*M*); ^b total energy (*E*); ^c aqueous solvation energy (*E*_{aq}); ^d solvation energy (*E*_{solv}); ^e dipole moment (μ); ^f energy of the HOMO orbital (*E*_{HOMO}); ^g energy of the LUMO orbital (*E*_{LUMO}); ^h area (*S*); ⁱ volume (*V*); ^j polar surface area (*PSA*); ^k ovality index (*OI*) (degree of deviation from perfect spherical shape molecule); ^l polarizability (α); ^m minimum value of electrostatic potential (*E*_{pot}).

3.2. Correlations between DFT-Calculated Frontier Molecular Orbital's Energies and Experimental Data

The calculated HOMO and LUMO energies were correlated with the experimental oxidation and reduction potentials. The last values were obtained from the electrochemistry experiments performed by differential pulse voltammetry (DPV), which is the most precise method used in our experiments to find the potential for a certain process. The experimental oxidation/reduction potential was assessed as the potential of the first anodic/cathodic DPV peak, denoted *E*_a and *E*_c, respectively. These values are listed in Table 3 for oxygen and sulfur derivatives. The data were collected in 0.5 mM solutions of each ligand in 0.1 M tetrabutylammonium perchlorate in acetonitrile [3–5,21,22]. The calculated

HOMO and LUMO energies (Table 1) were plotted against experimental oxidation and reduction potentials. Linear relationships were noticed. To this end, the reduction and oxidation potentials were correlated both with ionization potential (I) and electron affinity (A) computed using either $B3LYP$ or $\omega B97XD$ hybrid functionals. The parameters for the obtained linear correlations (a intercept, b slope, and R^2 correlation coefficient) are given in Table 4.

Table 2. Quantum chemical reactivity parameters of investigated compounds calculated using $B3LYP$ and $\omega B97XD$ DFT models.

Parameter	O1 C ₃₂ H ₂₉ NO ₂		O2 C ₃₀ H ₂₅ NO ₂		O3 C ₂₇ H ₁₉ NO ₂	
	<i>B3LYP</i>	$\omega B97XD$	<i>B3LYP</i>	$\omega B97XD$	<i>B3LYP</i>	$\omega B97XD$
$I^m = -E_{HOMO}$ (eV)	4.92	6.74	5.08	6.93	5.12	7.03
$A^n = -E_{LUMO}$ (eV)	1.79	0.13	1.77	0.13	2.04	0.36
$\Delta E_{gap}^o = I - A$ (eV)	3.13	6.61	3.31	6.8	3.08	6.67
$\chi^p = (I + A)/2$ (eV)	3.36	3.44	3.43	3.53	3.58	3.70
$\eta^q = (I - A)/2$ (eV)	1.57	3.31	1.66	3.40	1.54	3.34
$\sigma^r = 1/\eta$ (eV ⁻¹)	0.64	0.30	0.60	0.29	0.65	0.30
$\omega^s = \mu^2/2\eta$ (D ² ·eV ⁻¹)	3.07	1.62	3.55	1.98	2.75	1.45

Parameter	S1 C ₃₂ H ₂₉ NS ₂		S2 C ₃₀ H ₂₅ NS ₂		S3 C ₂₇ H ₁₉ NS ₂	
	<i>B3LYP</i>	$\omega B97XD$	<i>B3LYP</i>	$\omega B97XD$	<i>B3LYP</i>	$\omega B97XD$
$I^m = -E_{HOMO}$ (eV)	4.98	6.72	5.13	6.91	5.27	7.07
$A^n = -E_{LUMO}$ (eV)	1.84	0.14	1.83	0.14	2.06	0.36
$\Delta E_{gap}^o = I - A$ (eV)	3.14	6.58	3.30	6.77	3.21	6.71
$\chi^p = (I + A)/2$ (eV)	3.41	3.43	3.48	3.53	3.67	3.72
$\eta^q = (I - A)/2$ (eV)	1.57	3.29	1.65	3.39	1.61	3.36
$\sigma^r = 1/\eta$ (eV ⁻¹)	0.64	0.30	0.61	0.30	0.62	0.30
$\omega^s = \mu^2/2\eta$ (D ² ·eV ⁻¹)	3.08	1.58	3.36	1.86	2.42	1.19

^m ionization potential (I); ⁿ electron affinity (A); ^o energy gap (ΔE_{gap}); ^p electronegativity (χ); ^q global hardness (η); ^r softness (σ); ^s global electrophilicity index (ω).

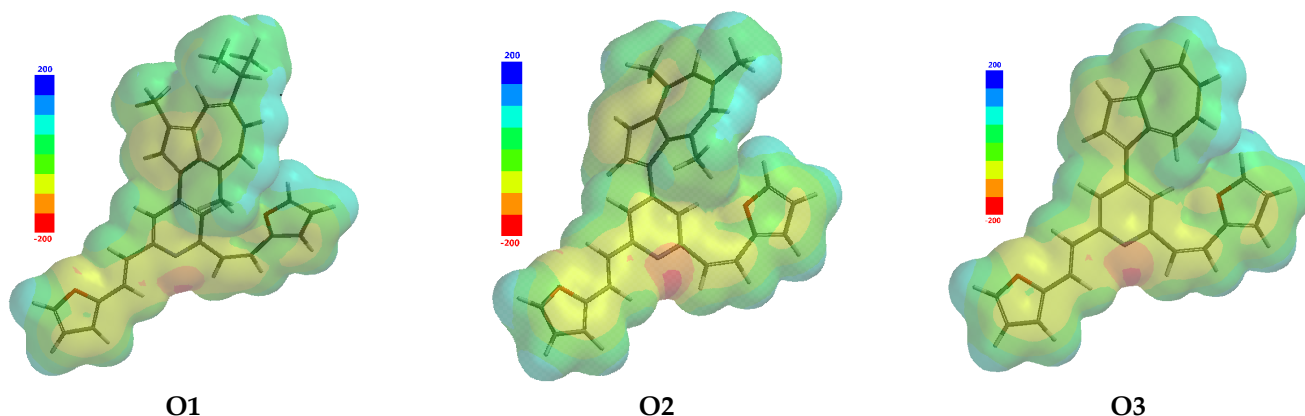


Figure 2. Predicted molecular electrostatic potential maps for O1–O3 compounds.

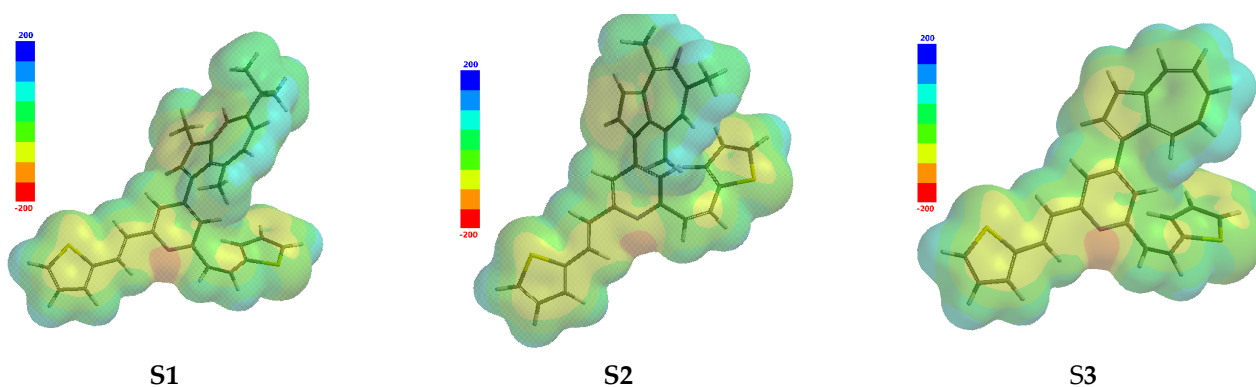


Figure 3. Predicted molecular electrostatic potential maps for S1–S3 compounds.

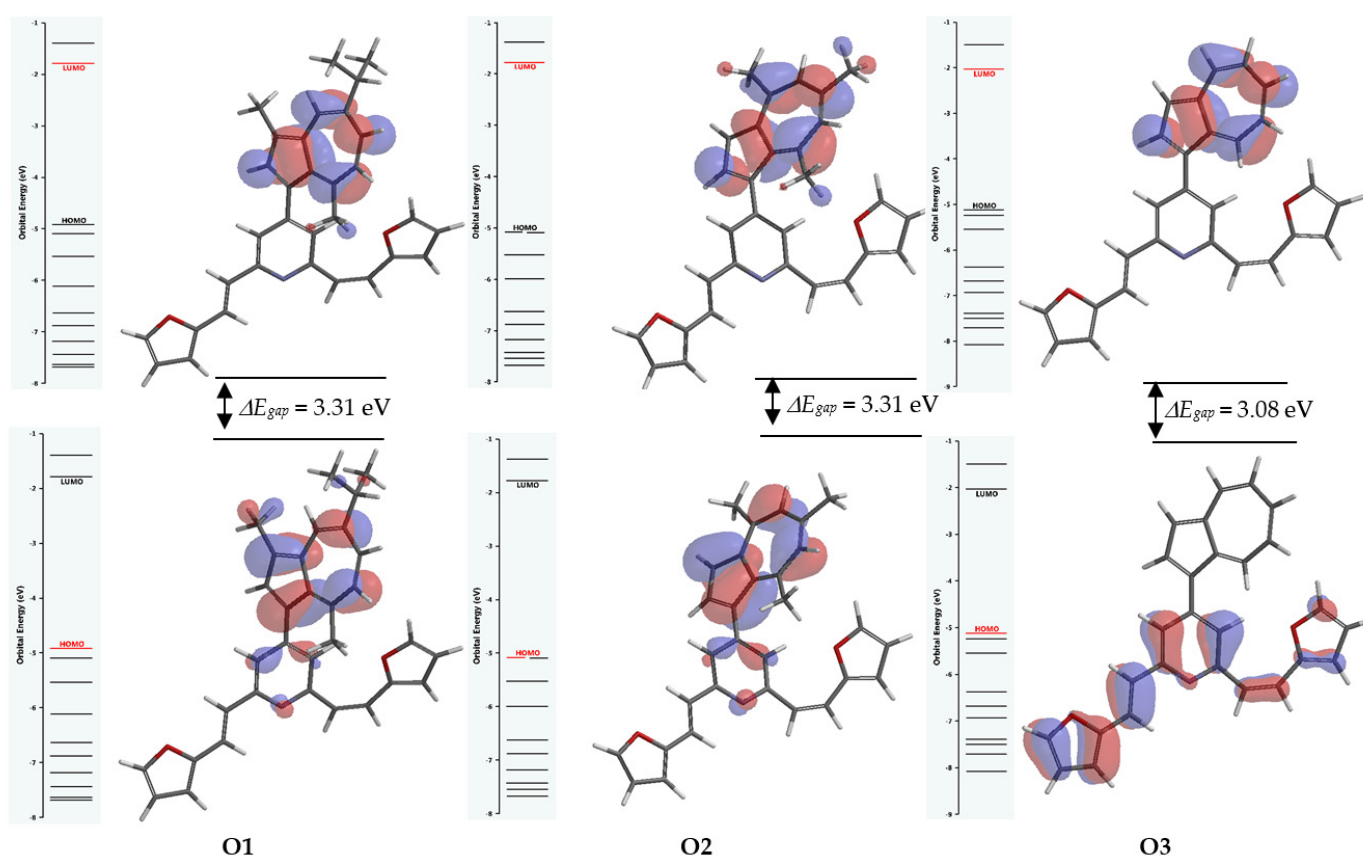


Figure 4. The frontier molecular orbitals diagram for O1–O3 computed using B3LYP/6-31G (d, p) level. The isovalues are referred to in Table 1.

3.3. Correlation between DFT-Computed Molecular and QSAR Properties and Ionization Potential or Electron Affinity

The correlations between computed molecular (E , E_{aq} , E_{solv} , μ) and QSAR (S , V , PSA , OI , α , E_{pot}) properties (from Table 1) and the ionization potential (I) or electron affinity (A) are shown in Tables 5 and 6, respectively. Linear relationships (a intercept, b slope, and R^2 correlation coefficient) were considered for most parameters.

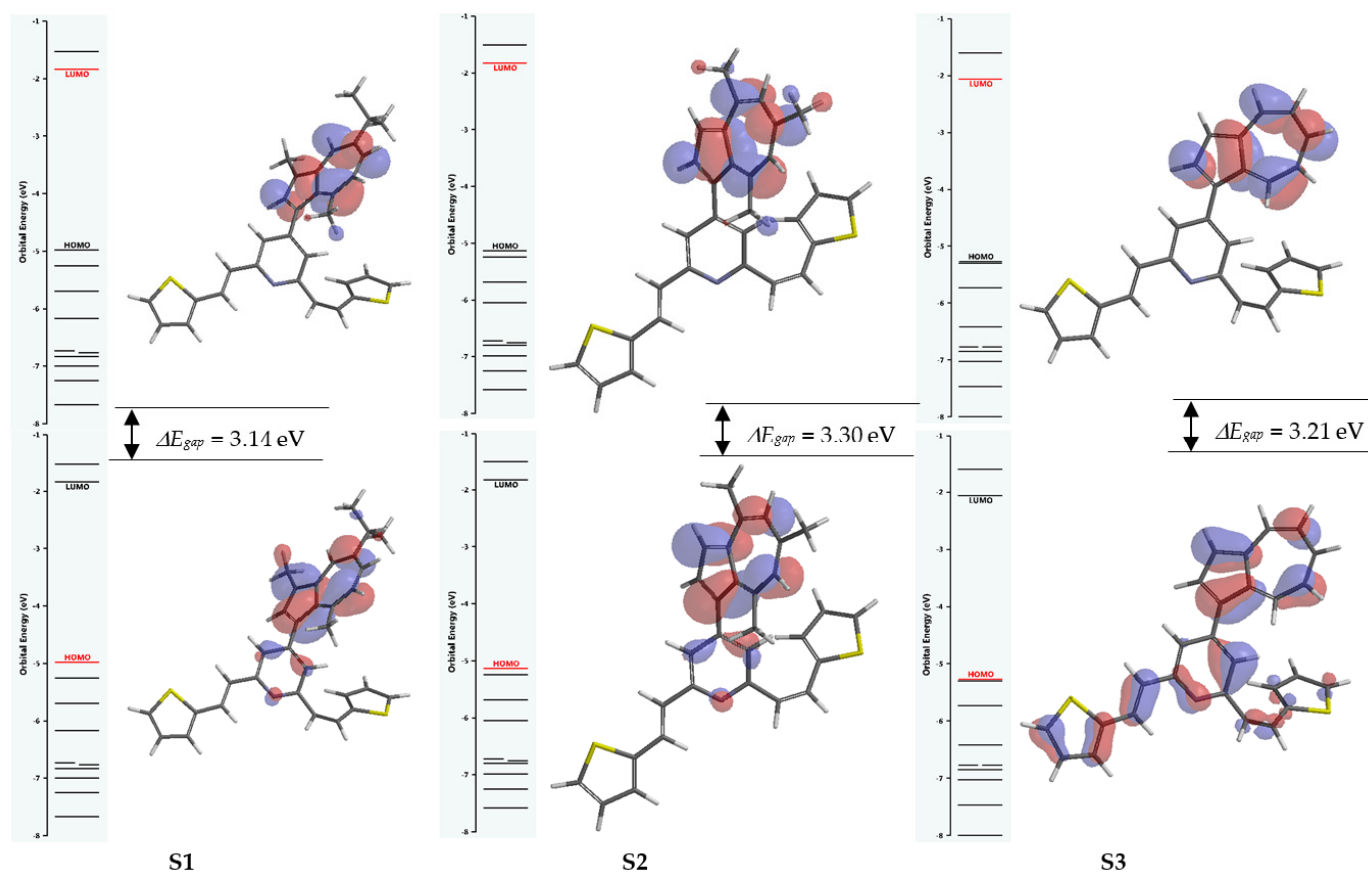


Figure 5. The frontier molecular orbitals diagram for **S1–S3** computed using *B3LYP/6-31G (d, p)* level. The isovalues are referred to in Table 1.

Table 3. Experimental oxidation (E_a) and reduction (E_c) potentials [3–5,21,22] for **O1–O3** and **S1–S3** ligands.

Property	Ligand		
	O1	O2	O3
E_a (V)	0.318	0.487	0.553
E_c (V)	−2.071	−2.084	−1.854
Reference	[4]	[2]	[22]
	S1	S2	S3
E_a (V)	0.338	0.470	0.567
E_c (V)	−2.065	−2.090	−1.858
Reference	[3]	[5]	[21]

Table 4. Values of intercept (a), slope (b), and correlation coefficient (R^2) from the linear correlation obtained for the oxidation (E_a) and reduction (E_c) potentials with I and A , respectively, for the investigated ligands from computations with *B3LYP* or ω *B97XD* hybrid functionals.

Correlation	<i>B3LYP</i>			ω <i>B97XD</i>		
	a	b	R^2	a	b	R^2
For O1–O3						
E_a vs. I	−5.298	1.141	0.993	−5.211	0.821	0.995
E_c vs. A	−3.606	0.859	0.9997	−2.204	0.972	0.998

Table 4. Cont.

Correlation	B3LYP			ω B97XD		
	<i>a</i>	<i>b</i>	R^2	<i>a</i>	<i>b</i>	R^2
For S1–S3						
E_a vs. <i>I</i>	4.500	1.259	0.995	6.202	1.523	0.999
E_c vs. <i>A</i>	3.949	1.017	0.996	2.199	0.991	0.990

Table 5. Linear correlations between predicted molecular properties and ionization potential (*I*) or electron affinity (*A*), computed using B3LYP and ω B97XD hybrid functionals; *A* and *I* are expressed in eV.

Correlation *	B3LYP			ω B97XD		
	<i>a</i>	<i>b</i>	R^2	<i>a</i>	<i>b</i>	R^2
For O1–O3						
<i>E</i> vs. <i>I</i>	−5595.9	842.39	0.812	−5786.5	642.99	0.917
<i>E</i> vs. <i>A</i>	−2441.8	584.77	0.791	−1491.1	683.54	0.842
E_{aq} vs. <i>I</i>	−5595.9	842.39	0.812	−5786.5	642.99	0.917
E_{aq} vs. <i>A</i>	−2441.8	584.77	0.791	−2441.8	584.77	0.791
E_{solv} vs. <i>I</i>	171.76	−39.66	0.870	178.07	−29.55	0.980
E_{solv} vs. <i>A</i>	19.12	−25.31	0.720	−19.95	−28.37	0.730
μ vs. <i>I</i>		nlc **			nlc **	
μ vs. <i>A</i>		nlc **			nlc **	
For S1–S3						
<i>E</i> vs. <i>I</i>	−5595.9	842.39	0.812	−5786.5	642.99	0.917
<i>E</i> vs. <i>A</i>	−3306.9	686.25	0.813	−2148.2	714.61	0.842
E_{aq} vs. <i>I</i>	−5461.9	676.00	0.982	−5838.5	556.91	0.973
E_{aq} vs. <i>A</i>	−3306.9	686.25	0.813	−2148.2	714.64	0.842
E_{solv} vs. <i>I</i>	93.18	−25.25	0.977	90.05	−18.27	0.936
E_{solv} vs. <i>A</i>		nlc **			nlc **	
μ vs. <i>I</i>		nlc **			nlc **	
μ vs. <i>A</i>	6.784	−1.941	0.863	3.745	−2.568	0.796

* The significance of the properties is the same as in Tables 1 and 2; ** nlc—nonlinear correlation.

Table 6. Linear correlations between predicted QSAR properties and ionization potential (*I*) or electron affinity (*A*), computed using B3LYP and ω B97XD hybrid functionals; *A* and *I* are expressed in eV.

Correlation *	B3LYP			ω B97XD		
	<i>a</i>	<i>b</i>	R^2	<i>a</i>	<i>b</i>	R^2
For O1–O3						
<i>S</i> vs. <i>I</i>	2460.50	−393.52	0.841	2541.00	−300.07	0.939
<i>S</i> vs. <i>A</i>	968.30	−263.11	0.760	534.35	−309.07	0.809
<i>V</i> vs. <i>I</i>	2422.40	−388.05	0.802	2494.20	−294.16	0.924
<i>V</i> vs. <i>A</i>	964.01	−266.49	0.782	528.54	−309.89	0.833
<i>PSA</i> vs. <i>I</i>		nlc **			nlc **	
<i>PSA</i> vs. <i>A</i>	16.19	1.18	0.969	16.15	4.94	0.999

Table 6. Cont.

Correlation *	B3LYP			ω B97XD		
	<i>a</i>	<i>b</i>	R^2	<i>a</i>	<i>b</i>	R^2
<i>OI</i> vs. <i>I</i>	3.89	−0.45	0.893	3.93	−0.33	0.969
<i>OI</i> vs. <i>A</i>	2.16	−0.28	0.690	1.69	−0.33	0.750
α vs. <i>I</i>	237.41	−31.54	0.826	242.59	−23.93	0.927
α vs. <i>A</i>	118.60	−21.50	0.776	82.66	−25.11	0.829
E_{pot} vs. <i>I</i>		nlc **			nlc **	
E_{pot} vs. <i>A</i>	−183.43	9.13	0.916	−170.90	20.15	0.959
For S1–S3						
<i>S</i> vs. <i>I</i>	2102.20	−314.06	0.991	2257.30	−256.31	0.990
<i>S</i> vs. <i>A</i>	1086.40	−311.13	0.781	556.15	−316.09	0.791
<i>V</i> vs. <i>I</i>	2074.80	−310.24	0.985	2233.80	−253.87	0.978
<i>V</i> vs. <i>A</i>	1081.30	−312.58	0.804	551.00	−323.02	0.832
<i>PSA</i> vs. <i>I</i>		nlc **		4.99	0.1782	0.959
<i>PSA</i> vs. <i>A</i>		nlc **		6.17	0.2341	0.870
<i>OI</i> vs. <i>I</i>	3.42	−0.345	0.999	3.61	−0.285	0.998
<i>OI</i> vs. <i>A</i>	2.28	−0.3254	0.716	1.71	−0.3409	0.750
α vs. <i>I</i>	209.18	−25.216	0.987	221.57	−20.678	0.979
α vs. <i>A</i>	128.29	−25.334	0.799	84.50	−26.25	0.829
E_{pot} vs. <i>I</i>		nlc **		−10.42	−21.099	0.923
E_{pot} vs. <i>A</i>		nlc **		−149.82	−29.00	0.917

* The significance of the properties is the same as in Tables 1 and 2; ** nlc—nonlinear correlation.

3.4. Correlation of Quantum Chemical Reactivity Parameters

The quantum chemical reactivity parameters of the investigated compounds obtained using B3LYP and ω B97XD hybrid functionals were also correlated with the ionization potential (*I*) or electron affinity (*A*). Linear correlations were proposed for each quantum chemical reactivity parameter, and the obtained correlation parameters (*a* intercept, *b* slope, and R^2 correlation coefficient) are given in Table 7 for each type of correlation.

Table 7. Linear correlations between predicted quantum chemical reactivity parameters and ionization potential (*I*) and electron affinity (*A*), respectively; *A* and *I* are expressed in eV.

Correlation *	B3LYP			ω B97XD		
	<i>a</i>	<i>b</i>	R^2	<i>a</i>	<i>b</i>	R^2
For O1–O3						
χ vs. <i>I</i>		nlc **			nlc **	
χ vs. <i>A</i>	2.0664	0.743	0.942	3.3624	0.9239	0.870
η vs. <i>I</i>	4.4667	−0.5714	1.000	5.1432	−0.2604	0.624
η vs. <i>A</i>		nlc **			nlc **	
σ vs. <i>I</i>	0.4941	0.2232	0.999	0.14	0.023	0.617
σ vs. <i>A</i>		nlc **			nlc **	
ω vs. <i>I</i>	21.971	−3.7393	0.954	14.382	−1.8404	0.999
ω vs. <i>A</i>		nlc **			nlc **	

Table 7. Cont.

Correlation *	B3LYP			ω B97XD		
	<i>a</i>	<i>b</i>	R^2	<i>a</i>	<i>b</i>	R^2
For S1–S3						
χ vs. <i>I</i>		nlc **			nlc **	
χ vs. <i>A</i>	1.6338	0.9867	0.948	3.3264	1.0795	0.893
η vs. <i>I</i>		nlc **			nlc **	
η vs. <i>A</i>		nlc **			nlc **	
σ vs. <i>I</i>		nlc **			nlc **	
σ vs. <i>A</i>		nlc **			nlc **	
ω vs. <i>I</i>	19.407	−3.2091	0.940	14.783	−1.9129	0.981
ω vs. <i>A</i>	9.6175	−3.4881	0.892	2.0581	−2.4249	0.823

* The significance of the properties is the same as in Table 2; ** nlc—nonlinear correlation.

4. Discussion

The calculated values given in Table 1, computed using B3LYP and ω B97XD hybrid functionals, are quite similar for E , E_{aq} , OI , α , and E_{pot} with those calculated with the B3LYP method, generally being slightly higher (in absolute value). Exceptions are observed for dipole moment (μ) and E_{HOMO} . Additionally, E_{solv} values for S1 and S2 are equal or lower when computed using B3LYP than ω B97XD.

The dipole moment (μ) for oxygen and sulfur compounds (Table 1) varies in the order: O2 > O1 > O3 and S2 > S1 > S3, respectively, which is the same order of variation for the absolute values of the minimum value of electrostatic potential (E_{pot}): O2 > O1 > O3 and S2 > S1 > S3 (Table 1). Both properties and quantities were used to describe the polarity of the molecule and indicate the unsubstituted compound as the least polar and the substituted ones (O2 and S2) as the most polar. The substitution of the hydrogen atoms in azulene by a methyl group or isopropyl group results in a systematic increase in the minimum value of electrostatic potential E_{pot} for both types of compounds, which can be explained by the +*I* inductive effects of alkyl groups.

The calculated values for quantum chemical reactivity parameters given in Table 2 predicted by B3LYP and ω B97XD are quite different. For the parameters I , ΔE_{gap} , χ , η , the values calculated with ω B97XD hybrid functional are significantly higher than those obtained from B3LYP computations (Table 2). For the parameters A , σ , and ω , the situation is reversed (Table 2). These findings apply to all oxygen and sulfur compounds.

Concerning ΔE_{gap} values, O3 reveals the smallest ΔE_{gap} and O2 the highest (Table 2). This can be explained by the substitution on the azulene ring by methyl or isopropyl groups (with +*I* inductive effects), which results in a systematic increase in the energy of the LUMO and an increase in the absolute value for the reduction potential.

Regardless of the method used for computation, it can be noticed that ionization potential (I) ranges in the order O1 < O2 < O3 (Table 1). The same behavior is observed for sulfur compounds (Table 1). The electron affinity values (A) do not show the same regular variation. The highest value of A is for O3; for O1 and O2, the values of A are relatively close (Table 1). For sulfur compounds, S3 has also the highest value for A , while for S1 and S2, the values of A are relatively close (Table 1).

Since our interest for these ligands is the complexation of the heavy metals ions, the donor–acceptor interactions were examined by different parameters: ΔE_{gap} , global electrophilicity index (ω), etc. The descriptor that was used to depict the molecular stability is the difference between HOMO and LUMO energy levels (ΔE_{gap}), which quantifies possible charge transfer interactions within the molecule. The higher the value of ΔE_{gap} , the more stable the compound is. The larger value of ΔE_{gap} for O2 and S2 in their homolog series leads to the conclusion that these substituted structures are more stable (Table 2).

Thus, the most reactive compounds seem to be the unsubstituted ones (**O3** and **S3**), which are more likely to be involved in the complexation process of HMs.

A molecule with a small ΔE_{gap} value is generally associated with low kinetic stability, high chemical reactivity, and high polarizability [46]. The unsubstituted compound **O3**, which has the smallest energy gap (Table 2), possesses the smallest polarizability (α), which means it is the most reactive (Table 1).

Further, the higher value of the global electrophilicity index ω (Table 2) for the substituted azulene compounds (**O2** and **S2**) suggests that they are more electrophilic than the unsubstituted compounds (**O3** and **S3**).

The graphical representations illustrated in Figures 2 and 3 indicate the chemically active regions and facilitate the comparison of the local reactivity sites of the investigated structures. The red area (negative charge) is found around the electronegative N in the pyridine, which indicates the reactive sites for the complexation process of these ligands upon HMs ions. The red region is susceptible to electrophilic attack. These negative areas correspond to the maximum negative values of potential (E_{pot} values from Table 1). The absolute E_{pot} values for oxygen compounds are ordered as follows: **O2** > **O1** > **O3**, regardless of the functional. For sulfur series, the order is similar for the *B3LYP* method (Table 1), that is, **S2** > **S1** > **S3**, and is slightly different for the ω *B97XD* hybrid functional (**S3** > **S2** > **S1**).

Comparatively, as expected, the oxygen compounds reveal more negative electrostatic potentials than sulfur compounds, as shown by the variation in the intensity of the red color (Figures 2 and 3).

The recently published molecules ((*Z*)-5-(azulen-1-ylmethylene)-2-thioxothiazolidin-4-ones) [26], with which our ligands share the azulene rings in common, as well as the same substituents to azulene, have smaller frontier orbital gaps, which means that they are more reactive than our **O1–O3** and **S1–S3** compounds. Thioxothiazolidin-4-one molecules also have a higher value of global electrophilicity index, with values around 5 D/(eV), compared with the investigated molecules (Table 2) with values around 3 D/(eV), suggesting that the corresponding ligands are more electrophilic than **O1–O3** and **S1–S3**, respectively.

The distribution of HOMO orbitals for oxygen compounds (Figure 3.3) is localized over azulene and pyridine rings for **O1** and **O2** compounds. For **O3**, they are localized on the conjugated system furan–vinyl–pyridine–vinyl–furan. For sulfur compounds (Figure 5), HOMO orbitals are distributed over azulene and pyridine rings for **S1** and **S2** compounds, and over the whole molecule in the case of **S3**. The difference between the distribution of HOMO orbitals in the case of **O1**, **O2**, and **O3** is a very important asset of the calculations, as they relate to the oxidation capacity of these ligands, which is a key parameter in these structures' electropolymerization.

For both oxygen and sulfur compounds, LUMO distribution is localized over azulene systems (Section 3.3 and Figure 5).

Considering our great interest in HMs ions recognition by complexation with the investigated ligands, we examined the donor–acceptor interactions. They can occur between the nitrogen lone pair and the vacant d orbital of the heavy metal.

The electrochemical oxidation and reduction potentials were read from the DPV curves, which indicate more precisely among the electrochemical methods the potentials of processes occurring during the anodic or cathodic scans. The electrochemical oxidation potentials (E_a) for both oxygen and sulfur compounds (Table 3) vary in the order **O3** > **O2** > **O1** and **S3** > **S2** > **S1**, respectively, indicating higher E_a values for the unsubstituted compounds, which are decreased by the presence of different substituents with +I inductive effects. The electrochemical reduction potentials E_c (in absolute value) for both oxygen and sulfur compounds (Table 3) vary in the reversed order than the oxidation potential: **O2** > **O1** > **O3** and **S2** > **S1** > **S3**, respectively. The substitution of the hydrogen atoms in azulene by methyl or isopropyl groups results in an increase in the absolute value of the reduction potential in respect to unsubstituted compound, but the regular behavior

is complicated by symmetry reasons, as **O2** is more symmetrical than **O1**, and its reduction is more difficult to occur.

E_{HOMO} and E_{LUMO} predicted chemical parameters (Table 1) were correlated with experimental electrochemical properties (Table 3). Linear relationships using both *B3LYP* and ω *B97XD* hybrid functions were obtained (Table 4). R^2 values indicate very good correlations between the calculated and the experimental values for both functionals (greater than 0.990).

The energies of the HOMO orbital follow the same order as the experimental values of the first anodic peak potentials E_a for oxygen and sulfur compounds—namely, **O3** > **O2** > **O1** and **S3** > **S2** > **S1** (absolute values). Thus, the evaluation of the oxidation capacity of the investigated azulenes is in good agreement with the electrochemical data.

The same order of variation for both E_a and E_c is observed for six similar compounds, derived from 4-(azulen-1-yl)-2,6-bis(2-furyl)- and 4-(azulen-1-yl)-2,6-bis(2-thienyl)-pyridines, that had been previously investigated [47].

Tables 5 and 6 show the correlations between calculated molecular properties (Table 1) and QSAR properties (Table 2) and the ionization potential (I) or electron affinity (A), respectively. Linear relationships were considered for all parameters, but we choose the correct connections using the best correlation coefficients (R^2). For instance, the R^2 value for the correlation of total energy (E) with I (0.917 in Table 5) is higher than for the corresponding correlation with A (0.842) when using the ω *B97XD* hybrid functional. Moreover, these values are greater than the ones obtained with the *B3LYP* method (0.812 and 0.791, respectively).

On the other hand, the R^2 value for the correlation of aqueous solvation energy (E_{aq} from Table 5) with A (0.791) is lower than the one for the correlation with I (0.917) when using the ω *B97XD* hybrid functional. When using the *B3LYP* method, both values are lower, 0.719 and 0.873, respectively. The same procedure was followed for all the other properties indicated in Table 1.

Table 8 shows the best correlations of the parameters (R^2 over 0.9) and the method used. For oxygen compounds, the best correlations were obtained using the ω *B97XD* hybrid functional. The dependencies with the ionization potential I are linear, except for PSA and E_{pot} , which are better correlated with A . For sulfur compounds, the best correlations were obtained with I , most of them using the *B3LYP* method.

Table 7 shows the linear correlations for quantum chemical reactivity parameters from Table 2, with A and I , respectively. For oxygen compounds, the correlations of η , σ , and ω are better with I than with A , while the correlation χ (A) is better than χ (I). The best correlation coefficient is obtained through the *B3LYP* hybrid functional. For sulfur compounds, the correlations are even worse than those for oxygen compounds. Therefore, good correlations were found only for χ (A) and ω (I), when using the *B3LYP* hybrid functional. The ω *B97XD* hybrid functional has a good correlation only for ω (I) for both oxygen and sulfur compounds. Table 9 shows the best correlations of the parameters (R^2 over 0.9) and the method used to get them.

Table 8. Linear correlations between molecular and QSAR properties * and I or A using best-performing DFT method; A and I are expressed in eV.

Correlated Parameters	a	b	R^2	DFT Method
Oxygen compounds				
E vs. I	−5786.5	642.99	0.917	ω <i>B97XD</i>
E_{aq} vs. I	−5786.5	642.99	0.917	ω <i>B97XD</i>
E_{solv} vs. I	178.07	−29.55	0.980	ω <i>B97XD</i>
S vs. I	2541.00	−300.07	0.939	ω <i>B97XD</i>
V vs. I	2494.20	−294.16	0.924	ω <i>B97XD</i>
PSA vs. A	16.15	4.94	0.999	ω <i>B97XD</i>
OI vs. I	3.93	−0.33	0.969	ω <i>B97XD</i>

Table 8. Cont.

Correlated Parameters	<i>a</i>	<i>b</i>	<i>R</i> ²	DFT Method
α vs. <i>I</i>	242.59	−23.93	0.927	ω B97XD
E_{pot} vs. <i>A</i>	−170.90	20.15	0.959	ω B97XD
Sulfur compounds				
<i>E</i> vs. <i>I</i>	−5461.8	676.00	0.982	B3LYP
E_{aq} vs. <i>I</i>	−5461.9	676.00	0.982	B3LYP
E_{solv} vs. <i>I</i>	93.18	−25.25	0.977	B3LYP
<i>S</i> vs. <i>I</i>	2102.20	−314.06	0.991	B3LYP
<i>V</i> vs. <i>I</i>	2233.80	−253.87	0.985	B3LYP
<i>PSA</i> vs. <i>I</i>	4.99	0.1782	0.959	ω B97XD
<i>OI</i> vs. <i>I</i>	3.42	−0.345	0.999	B3LYP
α vs. <i>I</i>	209.18	−25.216	0.987	B3LYP
E_{pot} vs. <i>I</i>	−10.42	−21.099	0.923	ω B97XD

* The significance of the properties is the same as in Table 1.

Table 9. Linear correlations between predicted quantum chemical reactivity parameters * and *I* or *A* using best-performing DFT method; *A* and *I* are expressed in eV.

Correlated Parameters	<i>a</i>	<i>b</i>	<i>R</i> ²	DFT Method
Oxygen compounds				
χ vs. <i>A</i>	2.0664	0.743	0.942	B3LYP
η vs. <i>I</i>	4.4667	−0.5714	1.000	B3LYP
σ vs. <i>I</i>	0.4941	0.2232	0.999	B3LYP
ω vs. <i>I</i>	21.971	−3.7393	0.954	B3LYP
ω vs. <i>I</i>	14.382	−1.8404	0.999	ω B97XD
Sulfur compounds				
χ vs. <i>A</i>	1.6338	0.9867	0.948	B3LYP
ω vs. <i>I</i>	19.407	−3.2091	0.940	B3LYP
ω vs. <i>I</i>	14.783	−1.9129	0.981	ω B97XD

* The significance of the properties is the same as in Table 2.

5. Conclusions

Quantum chemical calculations for azulenes substituted with thiophen- or furan-vinyl-pyridine showed that the predicted chemical parameters are correlated with the experimental electrochemical potentials. Linear relationships with the electron affinity (*A*) or ionization potential (*I*) were considered for the predicted molecular, QSAR properties, and quantum chemical reactivity parameters. For oxygen compounds, the dependencies of the molecular and QSAR properties with *I* (calculated with ω B97XD hybrid functional) are linear ($R^2 > 0.9$), except for *PSA* and E_{pot} , which are better correlated with *A*. For sulfur compounds, the best correlations were obtained with *I*, most of them by using the B3LYP method. For oxygen compounds, the dependencies of the quantum chemical reactivity parameters indicate better correlations of η , σ , and ω with *I* than with *A*, while the correlation χ (*A*) is better than χ (*I*). For sulfur compounds, good correlations were found only for χ (*A*) and ω (*I*), when using the B3LYP method.

The energies of the HOMO orbital follow the same order as the experimental values of the first anodic peak potentials. The same result was observed for the first cathodic peak potentials, which vary in the opposite direction, as expected. The redox potential is influenced by the number and position of the alkyl groups. Linear dependencies of DFT-computed energies of FMO and the experimental oxidation and reduction potentials were found. This computational study proves to be a good alternative approach to determine valuable parameters if we want to assess whether a certain ligand is good for a certain application. Both used density hybrid functionals give reliable results for properties computations and correlations and, therefore, are useful tools to further assess electrochemical applications. Thus, it is challenging to choose the preferred calculation hybrid functional.

Author Contributions: Conceptualization, E.-M.U., A.S. and O.C.; methodology, A.S.; software, A.S.; validation, O.C. and E.-M.U.; formal analysis, A.-A.V.; investigation, A.-A.V.; resources, E.-M.U.; writing—review and editing, E.-M.U., A.S. and O.C.; visualization, A.S.; supervision, E.-M.U. All authors have read and agreed to the published version of the manuscript.

Funding: This research received no external funding.

Conflicts of Interest: The authors declare no conflict of interest.

References

1. Ungureanu, E.-M.; Popescu, M.; Tatu, G.-L.; Birzan, L.; Isopescu, R.; Stanciu, G.; Buica, G.-O. Electrochemical Comparison on New (Z)-5-(Azulen-1-Ylmethylene)-2-Thioxo-Thiazolidin-4-Ones. *Symmetry* **2021**, *13*, 588. [CrossRef]
2. Oprisanu, A.; Matica, O.-T.; Ungureanu, E.M.; Cristea, M.; Birzan, L. Electrochemical study of azulene-pyridine compounds and film formation. *UPB Sci. Bull. Series B* **2022**, in press.
3. Oprisanu, A.; Lazar, I.G.; Pop, M.D.; Ungureanu, E.M.; Isopescu, R.; Birzan, L. Polyazulenes Based Materials for Heavy Metal Ions Detection. *Rev. Chim.* **2017**, *68*, 2215–2218. [CrossRef]
4. Pop, M.D.; Anastasoiaie, V.; Apostoiu Popescu, M.; Oprisanu, A.; Ungureanu, E.-M.; Cristea, M. New Azulene Modified Electrodes for Heavy Metal Sensing. *Rev. Chim.* **2017**, *68*, 2172–2175. [CrossRef]
5. Lazar, I.-G.; Diacu, E.; Ungureanu, E.-M.; Buica, G.-O.; Birzan, L.; Arnold, G.-L. Modified Electrodes Based on 2,6-Bis((E)-2-(Thiophen-2-yl)Vinyl)-4-(4,6,8-Trimethylazulen-1-yl)Pyridine For Heavy Metals Sensing. *UPB Sci. Bull. Ser. B.* **2017**, *79*, 23–36.
6. Engwa, G.A.; Ferdinand, P.U.; Nwalo, F.N.; Unachukwu, M.N. Mechanism and Health Effects of Heavy Metal Toxicity in Humans. In *Poisoning in the Modern World, New Tricks for an Old Dog?* Karcioğlu, O., Arslan, B., Eds.; IntechOpen: London, UK, 2019; ISBN 978-1-83880-786-3.
7. Posadas, Y.; López-Guerrero, V.E.; Segovia, J.; Perez-Cruz, C.; Quintanar, L. Dissecting the copper bioinorganic chemistry of the functional and pathological roles of the prion protein: Relevance in Alzheimer’s disease and cancer. *Curr. Opin. Chem. Biol.* **2022**, *66*, 102098. [CrossRef]
8. Gupta, R.; Kumar, P. Integrative analysis of OIP5-AS1/miR-129-5p/CREBBP axis as a potential therapeutic candidate in the pathogenesis of metal toxicity-induced Alzheimer’s disease. *Gene Rep.* **2022**, *26*, 101442. [CrossRef]
9. Huat, T.J.; Camats-Perna, J.; Newcombe, E.A.; Valmas, N.; Kitazawa, M.; Medeiros, R. Metal Toxicity Links to Alzheimer’s Disease and Neuroinflammation. *J. Mol. Biol.* **2019**, *431*, 1843–1868. [CrossRef]
10. Azevedo, J.A.; Azevedo, R.A. Heavy metals and oxidative stress: Where do we go from here? *Commun. Biometry Crop. Sci.* **2006**, *1*, 135–138.
11. Pratt, J.M. Metalloenzymes as Molecular Switches: The Role of Conformation Changes in Controlling Activity. *J. Inorg. Biochem.* **1986**, *28*, 145–153. [CrossRef]
12. Huang, J.; Huang, S.; Zhao, Y.; Feng, B.; Jiang, K.; Sun, S.; Ke, C.; Kymakis, E.; Zhuang, X. Azulene-Based Molecules, Polymers, and Frameworks for Optoelectronic and Energy Applications. *Small Methods* **2020**, *4*, 2000628. [CrossRef]
13. Razus, A.C.; Nica, S.; Cristian, L.; Raicopol, M.; Birzan, L.; Dragu, A.E. Synthesis and physico-chemical properties of highly conjugated azo-aromatic systems. 4-(azulen-1-yl)-pyridines with mono- and bis azo-aromatic moieties at C3-position of azulene. *Dye. Pigm.* **2011**, *91*, 55–61. [CrossRef]
14. Xin, H.; Li, J.; Lu, R.Q.; Gao, X.; Swager, T.M. Azulene–Pyridine-Fused Heteroaromatics. *J. Am. Chem. Soc.* **2020**, *142*, 13598–13605. [CrossRef] [PubMed]
15. Murfin, L.C.; Lewis, S.E. Azulene-A Bright Core for Sensing and Imaging. *Molecules* **2021**, *26*, 353. [CrossRef] [PubMed]
16. Xin, H.; Gao, X. Application of azulene in constructing organic optoelectronic materials: New tricks for an old dog. *ChemPlusChem* **2017**, *82*, 945–956. [CrossRef]
17. Amir, E.; Murai, M.; Amir, R.J.; Cowart, J.S.; Chabiny, M.L.; Hawker, C.J. Conjugated oligomers incorporating azulene building blocks—seven-vs. five-membered ring connectivity. *Chem. Sci.* **2014**, *5*, 4483–4489. [CrossRef]
18. Algohary, A.M.; Hassan, M.M.; El-Hashash, M.A.; Rizk, S.A.; Elamin, M.B.; Ahmed, A.H. Novel colorimetric chemosensors containing pyridine moiety for detection of some cations in water and crops samples: Design, synthesis, and evaluation. *J. Saudi Chem. Soc.* **2021**, *25*, 101386. [CrossRef]
19. Razus, A.C.; Birzan, L.; Pavel, C.; Lehadus, O.; Corbu, A.; Chiraleu, F.; Enache, C. Azulene-substituted pyridines and pyridinium salts. Synthesis and structure. 1. Azulene-substituted pyridines. *J. Heterocycl. Chem.* **2007**, *44*, 245–250. [CrossRef]
20. Popa-Tudor, I.; Gugoasa, L.A.; Stefan-Van Staden, R.-I. Electrochemical Sensor for the Assay of Zinc Ions in Whole Blood Samples. *UPB Sci. Bull. Ser. B* **2019**, *81*, 103–108.
21. Brotea, A.G.; Matica, O.-T.; Musina, C.; Ungureanu, E.-M. Polyazulene-Based Materials based on 4-(azulen-1-yl)-2,6-bis((E)-2-(thiophen-2-yl)vinyl)pyridine for Heavy Metals Ions Detection. *UPB Sci Bull.* **2021**, in press.
22. Enache, O.-I.; Matica, O.-T.; Bujduveanu, M.-R.; Ungureanu, E.-M.; Cristea, M. Electrochemical properties of 2,6-bis((E)-2-(furan-2-yl)vinyl)-4-(azulen-1-yl)pyridine. *UPB Sci Bull.* **2021**, in press.
23. Zarrouk, A.; Zarrok, H.; Salghi, R.; Hammouti, B.; Al-Deyab, S.S.; Touzani, R.; Hadda, T.B. A theoretical investigation on the corrosion inhibition of copper by quinoxaline derivatives in nitric acid solution. *Int. J. Electrochem. Sci.* **2012**, *7*, 6353–6364.

24. Korichi, H.; Zouchoune, F.; Zendaoui, S.M.; Zouchoune, B.; Saillard, J.Y. The coordination chemistry of azulene: A comprehensive DFT investigation. *Organometallics* **2010**, *29*, 1693–1706. [[CrossRef](#)]
25. Verdal, N.; Rivera, S.A.; Hudson, B.S. Inelastic neutron scattering and periodic DFT studies of crystalline aromatic materials: Azulene. A test of ab initio methods. *Chem. Phys. Lett.* **2007**, *437*, 38–44. [[CrossRef](#)]
26. Vasile, A.-A.; Ungureanu, E.-M.; Stanciu, G.; Cristea, M.; Stefaniu, A. Evaluation of (Z)-5-(Azulen-1-ylmethylene)-2-thioxothiazolidin-4-ones Properties Using Quantum Mechanical Calculations. *Symmetry* **2021**, *13*, 1462. [[CrossRef](#)]
27. Boulkroune, M.; Ignatovich, L.; Muravenko, V.; Spura, J.; Chibani, A.; Jouikov, V. Correlation of the HOMO–LUMO gap in furyl and thienyl nitrones and nitroethenes with their electrochemical redox potentials. *Chem. Heterocycl. Compd.* **2014**, *49*, 1579–1588. [[CrossRef](#)]
28. Brovelli, F.; Rivas, B.L.; Bernède, J.C.; del Valle, M.A.; Díaz, F.R.; Berredjem, Y. Electrochemical and optical studies of 1,4-diaminoanthraquinone for solar cell applications. *Polym. Bull.* **2007**, *58*, 521–527. [[CrossRef](#)]
29. Wu, T.Y.; Tsao, M.H.; Chen, F.L.; Su, S.G.; Chang, C.W.; Wang, H.P.; Lin, Y.C.; Sun, I.W. Synthesis and Characterization of Three Organic Dyes with Various Donors and Rhodanine Ring Acceptor for Use in Dye-Sensitized Solar Cells. *J. Iran. Chem. Soc.* **2010**, *7*, 707–720. [[CrossRef](#)]
30. Méndez-Hernández, D.D.; Tarakeshwar, P.; Gust, D.; Moore, T.A.; Moore, A.L.; Mujica, V. Simple and accurate correlation of experimental redox potentials and DFT-calculated HOMO/LUMO energies of polycyclic aromatic hydrocarbons. *J. Mol. Model.* **2013**, *19*, 2845–2848. [[CrossRef](#)]
31. Chen, L.; Stüb, D.; Sukuba, I.; Schauperl, M.; Probst, M.; Maihom, T.; Kaiser, A. Performance of DFT functionals for properties of small molecules containing beryllium, tungsten and hydrogen. *Nucl. Mater. Energy.* **2020**, *22*, 100731. [[CrossRef](#)]
32. Shao, Y.; Molnar, L.F.; Jung, Y.; Kussmann, J.; Ochsenfeld, C.; Brown, S.T.; Gilbert, A.T.B.; Slipchenko, L.V.; Levchenko, S.V.; O'Neill, D.P.; et al. Advances in methods and algorithms in a modern quantum chemistry program package. *Phys. Chem. Chem. Phys.* **2006**, *8*, 3172–3191. [[CrossRef](#)] [[PubMed](#)]
33. Parr, R.G.; Yang, W. *Density Functional Theory of Atoms and Molecules*; Oxford University Press: Oxford, UK, 1989; Volume 16.
34. Lee, C.; Yang, W.; Parr, R.G. Development of the Colle-Salvetti correlation-energy formula into a functional of the electron density. *Phys. Rev. B* **1988**, *37*, 785–789. [[CrossRef](#)] [[PubMed](#)]
35. Hehre, W.J. *A Guide to Molecular Mechanics and Quantum Chemical Calculations*; Wavefunction, Inc.: Irvine, CA, USA, 2003.
36. Pritchard, B.P.; Altarawy, D.; Didier, B.; Gibbs, T.D.; Windus, T.L. A New Basis Set Exchange: An Open, Up-to-date Resource for the Molecular Sciences Community. *J. Chem. Inf. Model.* **2019**, *59*, 4814–4820. [[CrossRef](#)]
37. Chai, J.D.; Head-Gordon, M. Long-range corrected hybrid density functionals with damped atom–atom dispersion corrections. *Phys. Chem. Chem. Phys.* **2008**, *10*, 6615–6620. [[CrossRef](#)]
38. Neese, F. Prediction of molecular properties and molecular spectroscopy with density functional theory: From fundamental theory to exchange-coupling. *Coord. Chem. Rev.* **2009**, *253*, 526–563. [[CrossRef](#)]
39. Pearson, R.G. Absolute electronegativity and hardness: Application to inorganic chemistry. *Inorg. Chem.* **1988**, *27*, 734–740. [[CrossRef](#)]
40. Yankova, R.; Genieva, S.; Halachev, N.; Dimitrova, G. Molecular structure, vibrational spectra, MEP, HOMO-LUMO and NBO analysis of Hf(SeO₃)(SeO₄)(H₂O)₄. *J. Mol. Struct.* **2016**, *1106*, 82–88. [[CrossRef](#)]
41. Pearson, R.G. Recent Advances in the Concept of Hard and Soft Acids and Bases. *J. Chem. Educ.* **1987**, *64*, 561–567. [[CrossRef](#)]
42. Wang, H.; Wang, X.; Wang, H.; Wang, L.; Liu, A. DFT study of new bipyrazole derivatives and their potential activity as corrosion inhibitors. *J. Mol. Model.* **2007**, *13*, 147–153. [[CrossRef](#)]
43. Parr, R.G.; Szentpaly, L.; Liu, S. Electrophilicity Index. *J. Am. Chem. Soc.* **1999**, *121*, 1922–1924. [[CrossRef](#)]
44. Vennila, P.; Govindaraju, M.; Venkatesh, G.; Kamal, C. Molecular structure, vibrational spectral assignments (FT-IR and FT-RAMAN), NMR, NBO, HOMO-LUMO and NLO properties of O-methoxybenzaldehyde based on DFT calculations. *J. Mol. Struct.* **2016**, *1111*, 151–156. [[CrossRef](#)]
45. Alam, M.J.; Ahmad, S. Anharmonic vibrational studies of L-aspartic acid using HF and DFT calculations. *Spectrochim. Acta A Mol. Biomol. Spectrosc.* **2012**, *96*, 992–1004. [[CrossRef](#)] [[PubMed](#)]
46. Demir, P.; Akman, F. Molecular structure, spectroscopic characterization, HOMO and LUMO analysis of PU and PCL grafted onto PEMA-co-PHEMA with DFT quantum chemical calculations. *J. Mol. Struct.* **2017**, *1134*, 404–415. [[CrossRef](#)]
47. Ungureanu, E.M.; Buica, G.O.; Razus, A.C.; Birzan, L.; Weisz, R.; Bujduveanu, M.R. Electrochemical study on 4-(azulen-1-yl)-2,6-bis (2-furyl)-and 4-(azulen-1-yl)-2,6-bis (2-thienyl)-pyridines. *Rev. Chim.* **2012**, *63*, 27–33.